ELSEVIER

Physica C 224 (1994) 300-316

PHYSICA C

Electron-doped and hole-doped infinite layer $Sr_{1-x}CuO_{2-\delta}$ films grown by laser molecular beam epitaxy

R. Feenstra *[,a,1], X. Li [b], M. Kanai [b], T. Kawai [b], S. Kawai [b], J.D. Budai [a], E.C. Jones [a], Y.R. Sun [a,c], J.R. Thompson [a,c], S.J. Pennycook [a], D.K. Christen [a]

[a] *Solid State Division, Oak Ridge National Laboratory, PO Box 2008, Oak Ridge, TN 37831-6057, USA*
[b] *Institute of Scientific and Industrial Research, Osaka University, 8-1 Mihogaoka, Ibaraki, 567 Osaka, Japan*
[c] *Department of Physics, University of Tennessee, Knoxville, TN 37996-1200, USA*

Received 23 December 1993; revised manuscript received 24 February 1994

1. Introduction

Comprising a simple oxygen deficient perovskite unit cell, the so-called "parent" or "infinite layer" $ACuO_2$ structure (see inset of Fig. 3) is the simplest structure containing the CuO_2 sheets essential for high-temperature superconductivity [1,2]. Basically all of the presently known superconducting cuprates may be structurally derived from the $ACuO_2$ structure by the insertion of chemically distinct metal oxide lattice planes parallel to the CuO_2 sheets, giving rise to a structural and chemical modulation along the common tetragonal *c*-axis [3-6]. Although not active themselves as superconducting layers, the intermediary oxide layers play a crucial role in establishing the onset of superconductivity by injecting charge carriers into the CuO_2 sheets. Depending on the lattice symmetry and insertion periodicity of the oxide "charge reservoir" layers, the Cu atoms are either four-, five-, or six-fold coordinated by oxygen, giving rise to a range of doping mechanisms as well as structure–superconductivity correlations.

$Sr_{1-x}(AE)_xCuO_2$ infinite layer compounds with AE = Ca or Ba can be synthesized over a wide range of alkaline-earth solid solutions, either by high-pressure, high-temperature sintering [7], or by epitaxy on a suitably lattice matched substrate (e.g. the (100) surface of $SrTiO_3$) using optimized oxide film deposition techniques [8-13]. The resulting compounds generally are metastable and insulating at the stoichiometric composition. The structure can be chemically doped, however, to become an electron-doped superconductor with $T_c \approx 40$ K by partial (10%-15%) substitution of a large rare earth (RE) species such as La, Pr, Nd, Sm, or Gd for Sr [14-16]. Alternatively, vacancies may be incorporated on the A lattice site according to the structure formula $(Sr_{1-x}(AE)_x)_{1-y}CuO_{2-\delta}$ and bulk superconductivity with $T_c \approx 60$–110 K has been observed for $y \approx 0.05$–0.2 in Ca and Ba solid solutions, as well as the end member containing only Sr ($x = 0$) [17-20].

The much higher T_c values for the AE deficient materials suggest that the superconductivity results from hole doping, similar to the structurally related high-T_c phases of the Bi-, Tl-, and Hg-based cuprate series. However, the detailed nature of the pertinent doping mechanism(s) has not yet been conclusively identified. A high density of planar defects parallel to the CuO_2 sheets has been observed in the AE deficient materials by high-resolution electron microscopy and their presence has been correlated with the

---

* Corresponding author.

[1] Research performed while on temporary assignment at the Institute of Scientific and Industrial Research, Osaka University, Japan.

SSDI 0921-4534(94)00100-T

onset of superconductivity [19–22]. It seems probable that the defect layers act as local charge reservoir layers for adjacent, unperturbed CuO_2 sheets, possibly changing the four-fold Cu–O coordination to five-fold as well. Thus superconductivity may be confined to a structure which locally may be regarded as a new, hole-doped superconducting compound [23]. Identification and isolation of these intergrowth phases is of great interest for a better understanding of the basic charge transfer mechanisms involved, as well as identification of the intrinsic superconducting properties of the parent $ACuO_2$ structure.

Based on this notion, this paper reports the growth and characterization of thin films of the simplest member of the potentially superconducting infinite layer cuprates, namely $Sr_{1-x}CuO_{2-\delta}$. The films were grown by atomic layer epitaxy using a hybrid laser ablation molecular beam epitaxy (laser-MBE) technique, with the intent to produce layered defect structures by adjustment of the Sr–CuO deposition scheme. Subsequently, the electrical properties of the as-grown films were studied as a function of the low temperature oxygen non-stoichiometry δ. It was observed that the films could be reversibly oxidized or reduced by annealing in mixed gas ambients with $p(O_2) \leqslant 1.0$ atm at temperatures below the growth temperature. Although the absolute value of δ in these experiments remains uncertain, the accompanying changes in carrier density provide important information regarding the *sign* of the majority charge carriers (holes or electrons) from the sense in which the electrical resistivity changes with $p(O_2)$. The present study may be considered a precursor to future attempts to synthesize new superconducting phases based on the infinite layer cuprate structure, focusing on correlations between growth, defect structures, and charge doping mechanisms.

The laser-MBE system used in this study recently was developed at Osaka University and optimized for application to the cuprate superconductors [8,9]. Combining the versatility of excimer laser ablation, e.g. with respect to source material selection and operation in reactive ambients, with the atomic layer control achievable by molecular beam epitaxy, the laser-MBE technique appears optimally suited for the atomic layer engineering of interfaces or planar defect structures. Little is known, however, about the atomistic processes controlling formation of the negatively charged CuO_2 sheets and ordering of the infinite layer structure during a layer-by-layer growth process. In the case of $Sr_{1-x}CuO_{2-\delta}$ films, for example, growth experiments using the simultaneous supply of both metallic constituents (co-deposition) indicate the existence of a net thermodynamic or kinetic driving force for formation of the infinite layer structure (on (100) $SrTiO_3$) under optimized conditions [11,12]. In a layer-by-layer deposition process, using similar synthesis conditions except for the sequential rather than simultaneous supply of the metallic constituents, these "spontaneous" effects could have a significant effect and counteract artificially imposed deviations in the oxide stacking sequence. Evaluation of the structural and electrical (superconducting) properties of films grown with different Sr–CuO deposition schemes, therefore, may provide useful information not only concerning the relation between charge doping and defect layers, but also concerning the layer-by-layer growth process itself.

This paper is organized as follows. Following a description of the laser-MBE system and other experimental techniques in section 2, section 3 describes the basic layer-by-layer growth experiments and the resulting *c*-axis epitaxial structure. A correlation is observed between the value of the *c*-axis lattice parameter and the X-ray diffraction intensity ratio (001)/(002) of the as-grown films. Results from the oxidation–reduction experiments will be presented in section 4. Remarkably, the oxygen exchange experiments indicate that the $Sr_{1-x}CuO_{2-\delta}$ films may be doped with either electrons or holes depending on the Sr–CuO deposition sequence employed, even without chemical substitutions. This qualitative difference in doping characteristics provides strong evidence for the effectiveness of the atomic layer epitaxy technique for the control of planar defect structures. A simple defect model is proposed (section 5) to explain this different behavior, in which we make the natural assumption that hole doping can occur only in the presence of apical Cu–O oxygen atoms, consistent with structure correlations for the presently known cuprate superconductors. The relation between growth and defect formation is further illustrated on the basis of this model. Conclusions are summarized in section 6. An Appendix describes our attempts to induce superconductivity in selected films that showed the strongest dependence of electrical properties on the oxygen content, by either vacuum or high-pressure oxygen annealing. A discussion is presented of the small hysteretic magnetic signals that may be observed for these films on $SrTiO_3$ substrates by high-sensitivity SQUID magnetometry.

2. Experimental

The $Sr_{1-x}CuO_{2\pm\delta}$ films were grown using the laser-MBE system developed at Osaka University by the sequential deposition of Sr(O) and CuO_x epitaxial overlayers on a (100) $SrTiO_3$ substrate (dimensions: $10\times5\times0.5$ mm^3) with continuous supply of a NO_2 gas flow impinging on the substrate (flow rate ~6 sccm). The NO_2 background pressure in the chamber was 10^{-5} mbar and, for all films reported in this paper, the substrate temperature measured with a pyrometer was maintained at 500 ± 10°C. Pulsed molecular beams of the constituent species were generated by ArF excimer laser ablation (193 nm) of a metallic Sr and sintered CuO target, respectively, mounted on a computer controlled carousel. The total beam energy was 200 mJ per pulse and the laser was operated at 1.1–2.2 pps. Typically, 25–30 laser pulses were needed for a Sr(O) monolayer and about 10–15 pulses for a CuO_x monolayer. The target–substrate spacing was approximately 10 cm.

The epitaxial overgrowth of the deposited layers was monitored by in situ reflection high-energy electron diffraction (RHEED), using an electron acceleration voltage of 15 kV. The RHEED patterns were collected on a phosphorous screen inside the vacuum chamber (base pressure 10^{-8} mbar) and subsequently recorded with a CCD camera for digitizing and computer-controlled spot analysis. A quartz crystal monitor adjacent to the substrate heater was available to monitor the instantaneous Sr or CuO deposition rates, however, as we will describe below, it was found more expedient to use the induced variations in the RHEED patterns instead to control the layer-by-layer growth process. Typical film thicknesses ranged from 70–400 Å. Following deposition, the films were rapidly cooled by turning off the substrate heater, leaving the NO_2 gas flow unchanged. Details of the laser-MBE and data collection systems have been described previously in refs. [8,24].

For several films, $Sr_{1-x}CuO_{2-\delta}$ film growth was initiated by the layer-by-layer deposition of a homoepitaxial $SrTiO_3$ buffer layer on the $SrTiO_3$ substrate. The targets used for this buffer layer comprised the same metallic Sr target as used for the $Sr_{1-x}CuO_{2-\delta}$ films and a sintered TiO_2 target. Monitoring of the induced RHEED specular intensity oscillations facilitated the preparation of a reproducible starting surface for the infinite layer cuprate film, indexed by either the maximum (after Sr deposition) or the minimum (after TiO_2 deposition) of a RHEED oscillation. Moreover, the shared use of the same Sr target provided useful information concerning the Sr ablation rate under the prevailing laser conditions during the initial stages of $Sr_{1-x}CuO_{2-\delta}$ film growth.

The epitaxial structure of the films was routinely characterized by X-ray diffraction (θ–2θ geometry), using a Cu Kα source and slits to collimate the beam. The samples were oriented with respect to the diffractometer such that approximately equal peak intensities were observed for the $SrTiO_3$ (001) reflection for each specimen. In these experiments the entire film was exposed to the X-ray beam for all orientations with $2\theta>10°$. Thus, a semi-quantitative comparison of relative (001) and (002) peak intensities was facilitated, providing information concerning the $Sr_{1-x}CuO_{2-\delta}$ defect structure [25]. Clear satellite peaks due to the finite film thickness were observed for most films near the principle diffraction peaks in the θ–2θ patterns, which proved useful for the calibration and fine tuning of the layer-by-layer growth process [26].

A more extensive characterization of the epitaxial structure for selected samples was performed using high-resolution four-circle diffractometry. The measurements were performed either at ORNL, using a Cu Kα source, LiF monochromator, and Ge (111) analyzer, or at the National Synchrotron Light Source, Brookhaven (beamline X14), using a Si(111) monochromator set to select $\lambda=1.5393$ Å X-rays, i.e. near the wavelength of Cu Kα. Two different modes were utilized at NSLS: a high-resolution mode with Si(111) analyzer after the sample and a low-resolution, high-intensity mode with only a slit between the sample and the detector.

The electrical transport properties were characterized by standard four-probe resistance measurements. The measurements were performed using spring loaded contact pins, pressed onto gold contact pads deposited on the film surface by sputtering through a shadow mask. In this way excessive contamination during subsequent low-temperature annealing could be avoided, while also a reproducible measurement geometry was provided by the gold contact pads. The reproducibility of the measured four-probe resistance between successive mounting–dismounting operations was better than ±3%. The temperature dependence of the resistance was measured in a continuous helium flow cryostat. A constant DC measuring current of 0.1–1 μA was used in combination with a high-impedance input range on the Keithley 181 nanovoltmeter. It was noted that measuring currents less than 0.1 μA for some films produced anomalous variations in the temperature dependent four-probe resistance, presumably because of incomplete compensation of thermal voltages. With the exception of the data presented in the Appendix of this paper, no anomalies were observed in the four-probe resistance at the indicated higher measuring currents.

The oxidation–reduction anneals were performed in a horizontal tubular furnace, fitted with a fused silica enclosure and equipped with an oxygen–argon mixing stage. The accessible oxygen partial pressure window with this annealing arrangement is $1.0 \geqslant p(O_2) \geqslant 3\times10^{-5}$ atm, as monitored with an Ametek S-3A oxygen analyzer at the furnace exit. The same equipment had previously been used for the processing and oxygen control of $YBa_2Cu_3O_{7-\delta}$ films [27]. A typical annealing cycle for the infinite layer $Sr_{1-x}CuO_{2-\delta}$ films consisted of: (i) rapid heating to 300°C in 10 min, (ii) a 1 h anneal at 300°C, and (iii) furnace cooling to 100°C in 30 min, after which the films were removed from the furnace. The resistance measurements usually were performed within hours of the low-temperature anneal. However, significant time dependent effects due to metastability or reaction with the ambient were not observed for any of the films, even after storage for days or weeks in a desiccator.

3. Layer-by-layer film growth and epitaxy

A sequence of characteristic RHEED patterns observed during the layer-by-layer growth of a $Sr_{1-x}CuO_{2-\delta}$ film is shown in Figs. 1(a)–(c). The patterns were obtained with the electron beam incident at a glancing angle with respect to the substrate surface and parallel to one of the in-plane [100] azimuths of the $SrTiO_3$ (001) substrate. Pattern 1a typically appeared after the deposition of approximately one monolayer of CuO (deposition sequence ··CuO–Sr–CuO). In addition to the principle [00], [01], and [02] diffraction rods coming from the $SrTiO_3$ substrate and film with in-plane lattice spacing $a=3.91$ Å, extra diffraction streaks are seen between the [01] and [02] diffraction rods. The intensity of these extra streaks depends on the amount of CuO deposited and the streaks disappear after deposition of a Sr(O) overlayer (Fig. 1(b), deposition sequence ··CuO–Sr–CuO–Sr). Simultaneous with the Sr and CuO depositions, distinct intensity variations of the specularly reflected electron beam along the [00] rod may be observed, the intensity increasing after Sr deposition and decreasing after CuO deposition (under standard conditions with substrate temperature 500°C and $p(NO_2) \approx 10^{-5}$ mbar).

Practically, the specular intensity variations and periodic appearances of the extra diffraction streaks provide a useful and accurate means for control of the layer-by-layer growth process. By monitoring both, it was found that the layer-by-layer growth process could be sustained over extended periods of time (up to 300 Sr–CuO deposition cycles) with apparently a stationary equilibrium between Sr and Cu atoms deposited and atoms incorporated into the infinite layer structure. The real-space origin of the additional incommensurate diffraction streaks, however, is presently unclear. The associated in-plane lattice spacing is $d=0.77a$ ($SrTiO_3$) ≈ 3.0 Å, which corresponds remarkably well to the nearest neighbor Cu–Cu distance along the [110] direction in Cu_2O, $d_{\text{Cu-Cu}} = (\sqrt{2}/2)a$ (Cu_2O). The corresponding Cu–O coordination is V-shaped, with two copper atoms sharing one oxygen atom. This suggests that the topmost CuO_x overlayer has not yet converted into a CuO_2 sheet as occurring in the infinite layer structure, but rather that a loosely bonded Cu-rich overlayer has formed which may react with subsequently incident Sr atoms to produce epitaxial growth of the infinite layer structure. Further research is ongoing to investigate these interesting phenomena.

A typical RHEED pattern after the deposition of a second Sr(O) monolayer is shown in Fig. 1(c) (deposition sequence ··CuO–Sr–CuO–Sr–Sr). In this case the principle diffraction rods have become somewhat diffuse and diffuse diffraction spots have developed along the [01] rods. The diffuse spots indicate that the second Sr(O) overlayer does not completely wet the underlying structure. The spots disappear, however, after the deposition of a next CuO monolayer (deposition sequence: ··CuO–Sr–CuO–Sr–Sr–CuO) to produce a RHEED pattern similar to Fig. 1(b), indicating that the surface has once again become flat (free of SrO islands). Upon continuation with Sr deposition, periodic oscillations between patterns 1b and 1c may be initiated, similar to the previously described oscillations between patterns 1a and 1b, albeit with less pronounced variations of the specular intensity. The resulting structure in both cases is of the infinite layer cuprate type, as measured by X-ray diffraction.

Upon continuation with a second CuO monolayer deposition instead of Sr (sequence: ··CuO–Sr–Sr–CuO–CuO), the incommensurate diffraction streaks reappear, just as before deposition of the double Sr and CuO overlayers (Fig. 1(a)). This observation suggests that the variations between patterns 1a and 1b are not intrinsically bound to depositions of precisely one monolayer of each of the constituents, but rather that different fractions of a monolayer may be deposited periodically, with constant Sr:CuO ratio. This remarkable property of the layer-by-layer growth process under the employed deposition conditions indicates a significant role of a spontaneous ordering mechanism for the infinite layer phase. In an extreme case of overlayer manipulation, it was observed that even when the Sr and CuO overlayer coverages repeatedly approached 2 ML, i.e. similar to the stacking sequence of the orthorhombic $SrCuO_2$ phase (which is more stable at ambient conditions), the predominant phase observed by X-ray diffraction nevertheless corresponded the tetragonal infinite layer phase. The detailed effect of different overlayer coverages on the defect formation will be discussed in section 5, following evaluation of the charge doping mechanisms.

It is interesting also to consider the effect of continued CuO deposition, i.e. beyond the point where the extra streaks in the RHEED pattern of Fig. 1(a) have become bright. In this case (with less than one extra

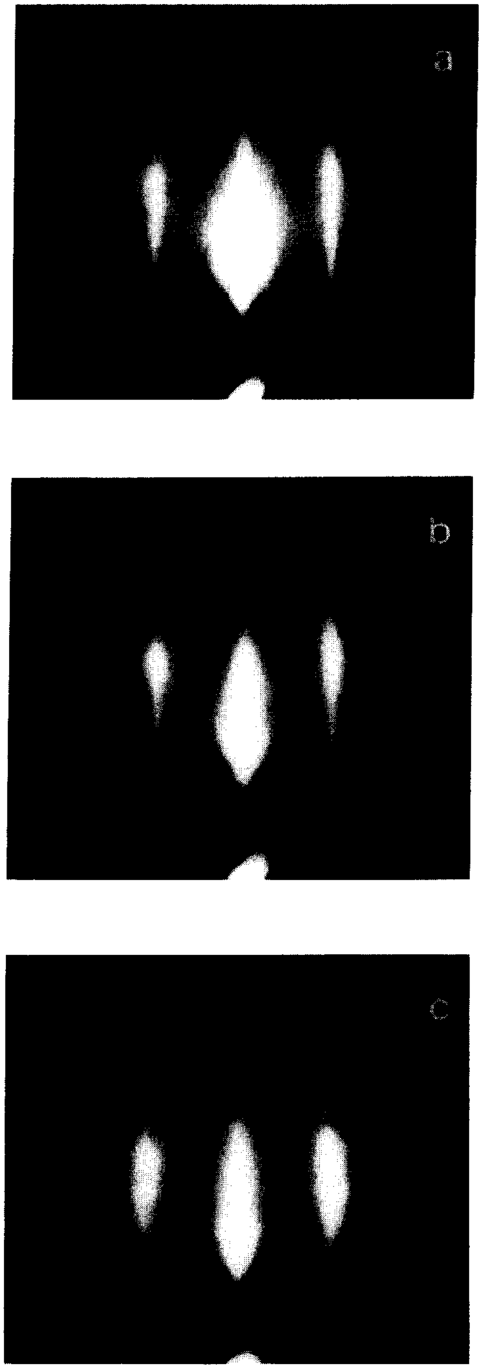

Fig. 1. Reflection high-energy electron diffraction (RHEED) patterns observed during the atomic layer-by-layer growth of infinite layer $Sr_{1-x}CuO_{2-\delta}$ films on a (001) $SrTiO_3$ substrate: (a) after deposition of a CuO monolayer; (b) after deposition of a Sr monolayer; (c) after deposition of two Sr monolayers. The incident electron beam is parallel to the $SrTiO_3$ in-plane [100] direction.

monolayer deposited) sharp diffraction spots suddenly appear in the RHEED pattern, indicating the formation of CuO_x islands. Contrary to the spots observed after extra Sr deposition (Fig. 1(c)), which dissolve after the deposition of extra CuO, the CuO_x related spots (and arcs) do not dissolve after additional Sr deposition. For this reason we assume that SrO_x double layers are formed more readily than CuO_x double layers during layer-by-layer growth, a result which we shall refer to later in this paper when discussing plausible defect structures in the $Sr_{1-x}CuO_{2-\delta}$ films.

X-ray diffraction confirmed formation of the infinite layer cuprate structure with the *c*-axis perpendicular to the substrate surface *for all films*, even if the Sr–CuO stacking sequence deviated markedly from the ideal 1:1 monolayer-by-monolayer sequence. As noted previously, we consider this observation strong evidence for the existence of a significant driving force for formation of the infinite layer structure under the employed deposition conditions. Weak extra diffraction peaks belonging to either the $Sr_{14}Cu_{24}O_{41}$ phase [28] or Sr_2CuO_3 [29] appeared when deviations in the Sr:Cu stoichiometry apparently became too large. The tendency for formation of these additional phases increased with increasing substrate temperature or reduced NO_2 supply. Overlayer coverages larger than one monolayer also promoted formation of secondary phases, although the infinite layer phase invariably constituted the dominant phase of the resulting epitaxial structure. For films grown at substrate temperatures lower than 480°C, the X-ray diffraction peaks weakened significantly, indicating that the processing range for the infinite layer structure is relatively narrow [9]. At these lower substrate temperatures, the contrast in the RHEED pattern during deposition also diminished rapidly.

Results from a detailed X-ray analysis performed at the Brookhaven NSLS facility for a $Sr_{1-x}CuO_{2-\delta}$ film grown under standard deposition conditions (500°C, $p(NO_2)=10^{-5}$ mbar) are shown in Figs. 2(a)–(d). Composition control for this film was achieved by optimization of the periodic variations in the RHEED pattern between Figs. 1(a) and 1(b). The low-resolution θ–2θ scan of Fig. 2(a) confirms formation of the infinite layer cuprate structure with the *c*-axis perpendicular to the substrate surface. The *c*-axis length calculated from the (001) and (002) reflections is 3.463 Å. A high-resolution θ–2θ scan of the (002) reflection (Fig. 2(b)) shows the typical interference pattern expected for a quasi-two-dimensional thin film [26]. The film thickness calculated from this interference pattern (297 ± 12 Å$\approx86\pm4$ unit-cell layers) corresponds well with the supplied number of Sr–CuO deposition cycles (~84). As a result of the high synchrotron beam intensity, two weak additional diffraction peaks were resolved in the θ–2θ diffraction scan, namely at $2\theta=13.14°$ and $31.13°$. The relative sharpness of these peaks indicates that the corresponding secondary phases (possibly $Sr_{14}Cu_{24}O_{41}$ in two orientations) are not intergrown along the *c*-axis of the infinite layer phase, but rather that small islands of these phases are present in the film.

The Φ-scan of Fig. 2(c) indicates that the infinite layer structure is in complete three-dimensional epitaxial registry with the $SrTiO_3$ substrate, and that essentially no other $Sr_{1-x}CuO_{2-\delta}$ in-plane orientations have formed. The epitaxial relation is as expected: $a_{SCO}\parallel[100]_{STO}$ and $c_{SCO}\parallel[001]_{STO}$. The (H 0 2) scan of Fig. 2(d) along the in-plane $SrTiO_3$ [100] direction confirms that the infinite layer structure is tetragonal. Peaks are observed only at integer intervals commensurate with the $SrTiO_3$ in-plane lattice spacing, from which it follows that $a_{SCO}=a_{STO}=3.905$ Å. Thus the *a*-axis of the $Sr_{1-x}CuO_{2\delta}$ film is slightly shorter than reported for (stoichiometric) $SrCuO_2$ bulk material (3.92 Å), whereas the *c*-axis is slightly longer (3.43 Å for bulk $SrCuO_2$ [7]). The close correspondence between the in-plane film and substrate spacings illustrates the important role of epitaxy in stabilizing the infinite layer structure in films, putting the $SrCuO_2$ structure under considerable compressive stress along the film–substrate interface. Less interfacial stress is expected for Ca-doped $Sr_{1-x}(AE)_xCuO_2$ compositions ($x\approx0.25$) since both the *a*- and *c*-axes decrease with Ca concentration [7].

In contrast to the single-crystal-like crystallographic properties described above, a closer examination of the (001) and (002) diffraction peaks in Fig. 2(a) suggests that the infinite layer structure, nevertheless, contains a high density of structural defects. This may be inferred from the ratio of the (001) and (002) peak intensities $X\equiv(001)/(002)$, which for a perfect, stoichiometric $SrCuO_2$ infinite layer structure may be calculated as $X\approx0.05$–0.07 [25].

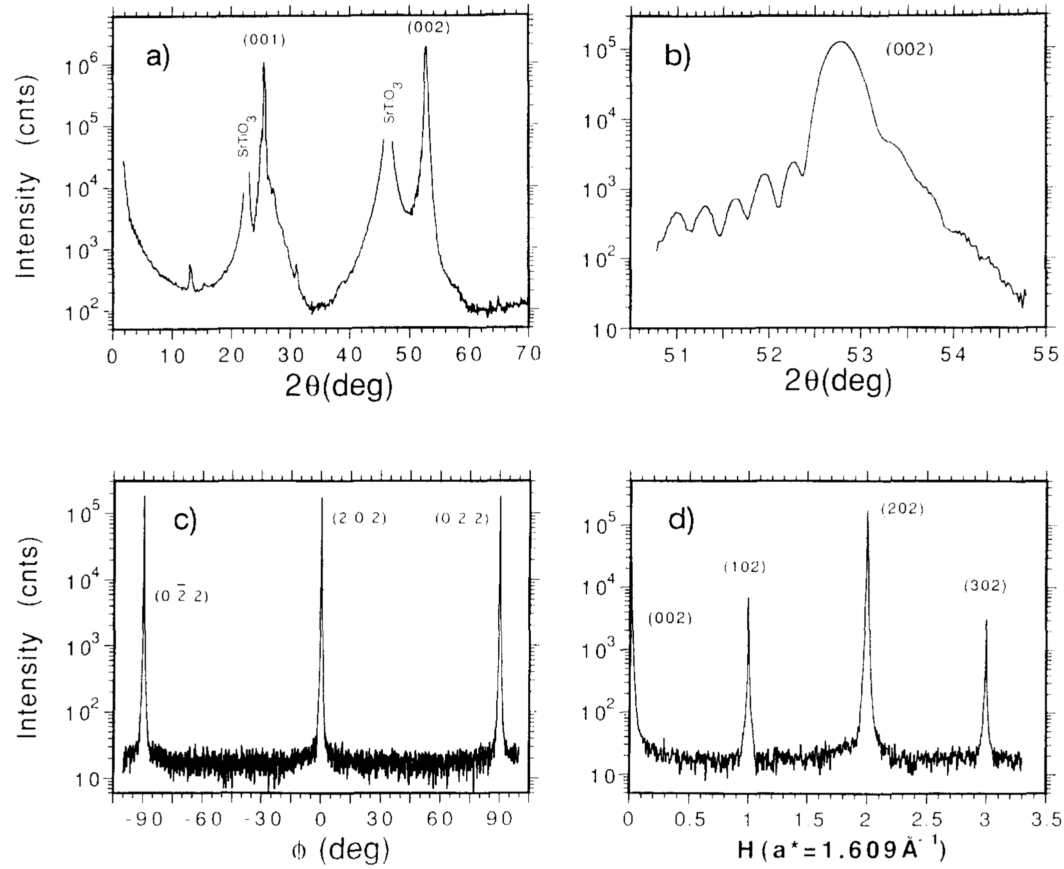

Fig. 2. X-ray diffraction patterns of a $Sr_{1-x}CuO_{2-\delta}$ film on (001) $SrTiO_3$ substrate measured at the Brookhaven National Synchrotron Light Source (Beamline X14): (a) low-resolution θ–2θ scan with diffraction vector parallel to the substrate [001] direction; (b) high-resolution θ–2θ scan of the film's (002) diffraction peak and finite size interference pattern; (c) Φ-scan around substrate [001] direction. $\phi = 0°$ corresponds to substrate in-plane [100] direction; (d) (H 0 2)-scan along substrate [100] direction. Units correspond to substrate reciprocal lattice constant $a^* = 2\pi(3.905)^{-1}$ (Å)$^{-1}$.

For the film of Fig. 2(a), however, $X \approx 0.5$ and a similar intensity ratio was observed in the standard, slit-collimated X-ray measurement.

The much larger intensity ratio indicates a significant Sr deficiency ($x \approx 0.3$ in $Sr_{1-x}CuO_{2-\delta}$ [25]) or the presence of planar defects (e.g. stacking faults) perpendicular to the c-axis. In particular, intergrowths giving rise to local expansions of the interplanar spacings by $c/4$ (~ 0.86 Å) or $c/2$ (~ 1.7 Å) could seriously affect the (001)/(002) intensity ratio through destructive interference of the diffracted X-ray beam, depending on density and distribution. On the other hand, since the Sr:Cu composition is not absolutely controlled in the present growth experiments, off-stoichiometry with respect to the Sr:Cu ratio could arise from natural tendencies towards Sr-vacancy incorporation [29]. Antisite disorder between Sr and Cu atoms also may contribute to an enhanced (001)/(002) intensity ratio; however, the estimated contribution is too small to fully explain the enhancement [25].

A comparison of (001)/(002) peak intensity ratios and corresponding c lattice spacings for a number of films is shown in Fig. 3. Films grown by periodic depositions of Sr and CuO overlayers as well as films containing "non-periodic" Sr and CuO depositions are included in this figure. For the majority of the periodically grown films, $0.2 < X < 0.4$, however, X-values as small as 0.1 and as large as 0.9 also were obtained. On the other hand, films containing delib-

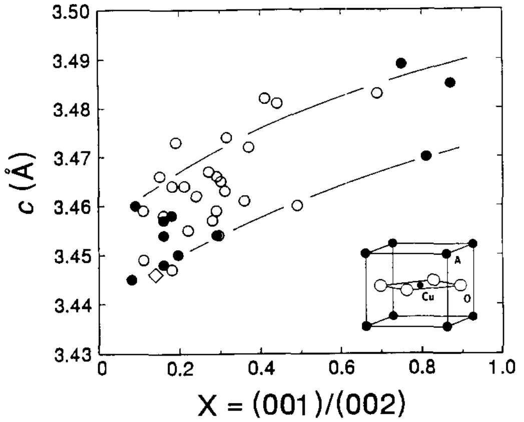

Fig. 3. Correlation between c-axis lattice parameter and (001)/(002) diffraction intensity ratio X for infinite layer $Sr_{1-x}CuO_{2-\delta}$ films with periodic and non-periodic atomic layering schemes. Closed symbols: hole-doped films, open symbols: electron-doped films and films with gradient $|Y| \leq 0.05$ (defined in text). Diamond: co-deposited $Sr_{0.9}CuO_{2-\delta}$ film. The lines are to guide the eye. The inset shows a schematic of the infinite layer $ACuO_2$ unit cell.

erately inserted defect layers typically had $X < 0.2$. As we will describe below these latter films generally exhibited hole-doping characteristics, indicated by the filled symbols in Fig. 3. Independent of the precise deposition sequence, however, the data in Fig. 3 suggest a trend between the c-axis length and the (001)/(002) intensity ratio. With increasing X, the c-axis expands from ~3.45 Å for $X \approx 0.1$ to $c \approx 3.48$ Å for films with $X \approx .0.8$.

This c-axis expansion is qualitatively consistent with the introduction of vacancies on the Sr-site: Sr vacancies may enhance the repulsive electrostatic interaction between the negatively charged CuO_2 sheets, giving rise to an expansion of the c-axis [19]. However, the expansion could be (partially) counteracted by oxygen vacancies in the CuO_2 sheets to maintain charge neutrality. Defect layers in which the Sr vacancies are clustered also are expected to expand the c-axis: Hiroi et al. [21] observed a local expansion of interplanar spacings of ~0.8 Å, surrounding planar defects characterized as a combination of two Sr-deficient layers separated by an oxygen-deficient $CuO_{2-\delta}$ sheet. The local expansions could contribute to a partial extinction of the (002) diffraction peak through destructive interference. It is interesting that both explanations, Sr point defects or Sr-deficient planar defects, entail a Sr-deficient composition of the infinite layer phase.

4. Oxidation–reduction experiments

The as-grown films uniformly exhibited semiconducting behavior of the resistivity ρ for $T < 300$ K, with room-temperature values ranging between ~0.1–10 Ω cm. Although anomalies in the temperature dependence of the resistivity, indicative for the onset of superconductivity in part of the film, were reported in previous work [30], similar anomalies were not observed in the present study for any of the films investigated. To examine whether the resistivity could be lowered by oxygen exchange, several films were annealed in oxygen ambients with $p(O_2) \leq 1.0$ atm at temperatures between 200°C and 700°C. An annealing temperature of 300°C emerged from these initial studies as a reasonably low processing temperature for reversible oxygen exchange, producing reversible changes in ρ with increasing or decreasing $p(O_2)$.

Temperature dependences of the resistivity for two films (films A and B) after annealing at oxygen pressures between 1.0 atm and $p(O_2) = 3 \times 10^{-5}$ atm ("argon") are shown in Figs. 4(a), (b). It is seen that, for both films, the resistivity varies significantly with the oxygen pressure, both in magnitude and temperature dependence. As expected, the resistivity curves at high temperatures become flatter with decreasing $\rho(300\text{ K})$; however, a clear onset of superconductivity is not observed even at the lowest resistivities reached. The most remarkable feature of Fig. 4, however, is that the lowest resistivities for either film were not obtained with the same oxygen treatment, but rather at opposite ranges of $p(O_2)$. For film B the resistivity decreased with increasing oxygen pressure (Fig. 4(b)), whereas for film A the resistivity increased (Fig. 4(a)). Thus, for film A the resistivity reached its lowest values after annealing in (undiluted) argon. This different behavior suggests the existence of *distinct defect structures* in either film, giving rise to dissimilar charge doping mechanisms. In particular, film B appears *hole-doped*, since addition of holes by oxygen absorption increases the conductivity. On the other hand, film A appears *elec-*

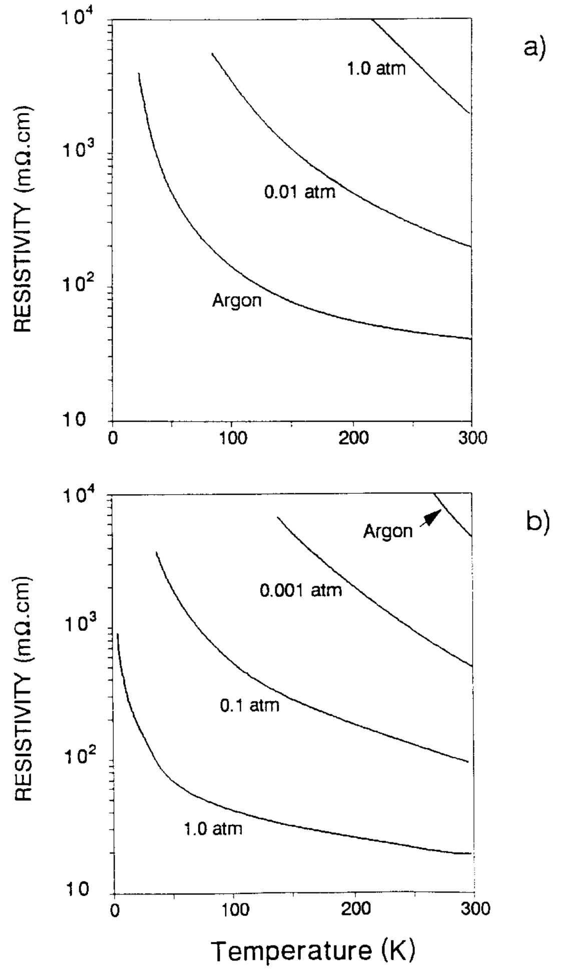

Fig. 4. Four-probe electrical resistivity as a function of temperature for two infinite layer $Sr_{1-x}CuO_{2-\delta}$ films: (a) film A; (b) film B (see Table 1). The resistivity curves were obtained after annealing at 300°C at the indicated oxygen partial pressures. The label "Argon" indicates an oxygen pressure of 3×10^{-5} atm.

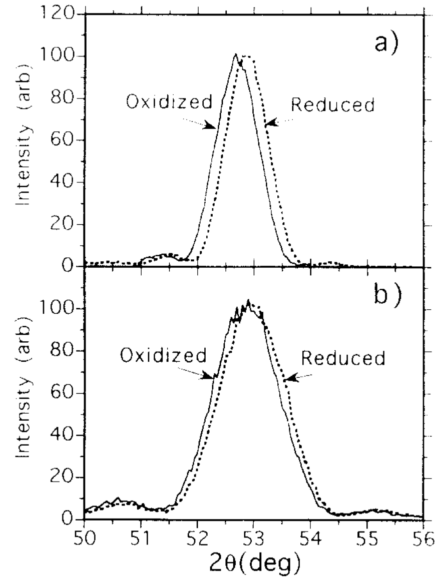

Fig. 5. High-resolution scan of the (002) diffraction peak showing shift after annealing in different oxygen ambients: (a) film A, first anneal in argon, second anneal in oxygen; (b) film B, first anneal in oxygen, second anneal in argon.

tron-doped, since in this case oxygen absorption decreases the conductivity.

Supporting evidence for the oxygen related nature of the annealing induced resistivity changes is provided by the observation of reversible changes in the *c*-axis lattice parameter. The *c*-axis variations are illustrated in Figs. 5(a), (b) for films A and B, respectively, in the form of high-resolution θ–2θ scans of the (002) diffraction peak. It is seen that for both films, annealing shifted the entire (002) diffraction peak while leaving the shape unchanged. These parallel shifts suggest a homogeneous variation of interplanar lattice spacings, consistent with a homogeneous variation of the oxygen non-stoichiometry. The shift in Fig. 5(a) corresponds to an expansion of the *c*-axis from 3.461 Å after annealing in argon, to 3.471 Å after annealing in oxygen. An opposite sequence of anneals was applied to film B in Fig. 5(b) to produce a contraction from $c=3.460$ Å after annealing in oxygen to 3.453 Å after annealing in argon, respectively. Thus, for both films the *c*-axis after oxidation is longer than after reduction, and the changes are reversible. Similar to the effect of Sr point defects, the *c*-axis expansion may be related to an enhanced electrostatic repulsion between the constituent lattice planes. For example, incorporation of oxygen between the CuO_2 sheets could enhance the repulsion between the sheets, whereas the filling of oxygen vacancies in the CuO_2 sheets would enhance the electrostatic repulsion between the intermediate Sr layers.

The reversibility of the annealing induced changes is further illustrated in Figs. 6(a)–(d), where we have plotted the value of the room-temperature resistivity $\rho(300\ K)$ as a function of $p(O_2)$ for films A and B and two other $Sr_{1-x}CuO_{2-\delta}$ films, both upon increasing and decreasing oxygen partial pressure. Although a small hysteresis was observed for most films, the annealing induced variations in $\rho(300\ K)$ were

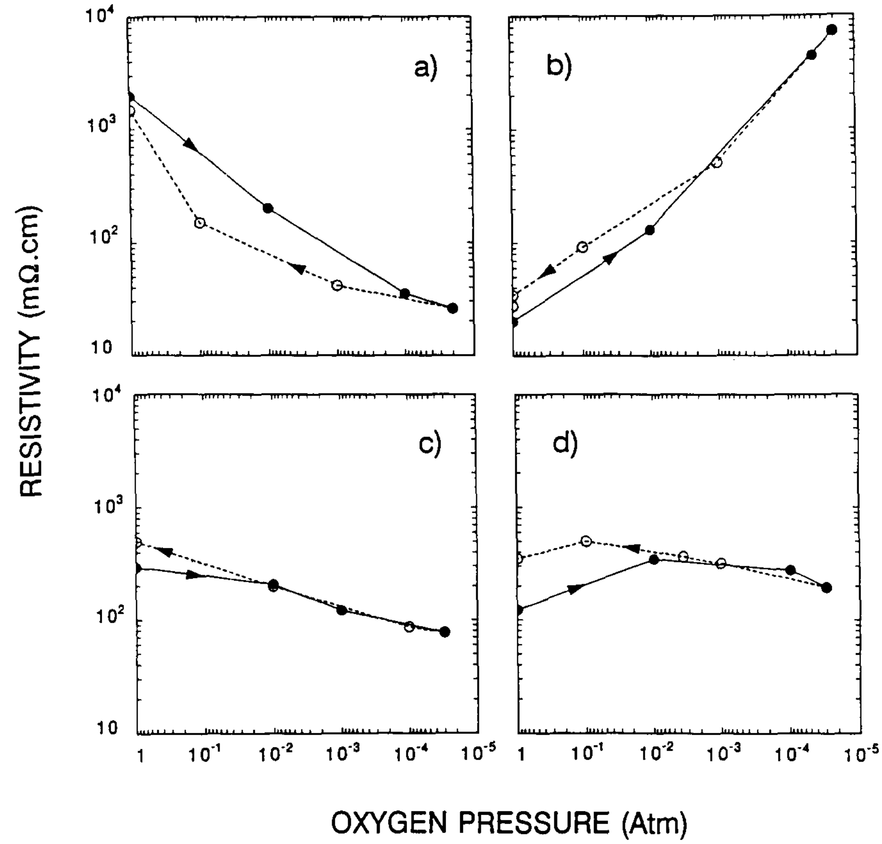

Fig. 6. Variation of the room-temperature resistivity ρ(300 K) with the oxygen partial pressure $p(O_2)$ during anneals at 300°C for infinite layer $Sr_{1-x}CuO_{2-\delta}$ films: (a) film A; (b) film B; (c) film C (see Table 1). Closed symbols and solid lines indicate variation with decreasing oxygen pressure; open symbols and broken lines indicate variation with increasing oxygen pressure.

essentially reversible in the oxygen pressure. We conclude that the 300°C anneals resulted primarily in reversible oxygen exchange, and therefore provide useful information regarding the effect of hole addition or removal on the pre-existing charge distribution. Since the pre-existing charge distributions in the infinite layer compound depend on the distribution of lattice defects, the oxygen induced variations in carrier density indirectly probe this defect structure.

The oxygen induced variations in ρ(300 K) with $p(O_2)$ for most films were monotonic with gradient $Y \equiv \mathrm{d}(\log \rho)/\mathrm{d}(\log p)$ either positive or negative, both upon oxygen absorption and desorption. Different gradients Y were observed for films of either kind, hole-doped or electron-doped (e.g. Fig. 6(c)). For a few films, however, the resistivity passed through a maximum as a function of $p(O_2)$, as illustrated in panel 6d. It is possible that for these latter films other structural changes also affect the resistivity. Alternatively, the peaked resistivity behavior could be the result of two opposing effects related to oxygen exchange, becoming apparent at different oxygen occupancies.

An overview of the different gradients Y for the series of films introduced in Fig. 3 is presented in Fig. 7. Here, Y is plotted against the room-temperature resistivity ρ(300 K), either after reduction in 0.0001 atm of oxygen (Fig. 7(a)), or after oxidation in 1.0 atm of oxygen (Fig. 7(b)). Note that in each of these panels the hole-doped films are located in the bottom part of the figure ($Y < 0$) and the electron-doped films ($Y > 0$) in the upper part. The films showing peaked behavior have been denoted by $Y = 0$.

A clear correlation is observed in Fig. 7(a), with the hole-doped films generally exhibiting higher resistivities after reduction than the electron-doped

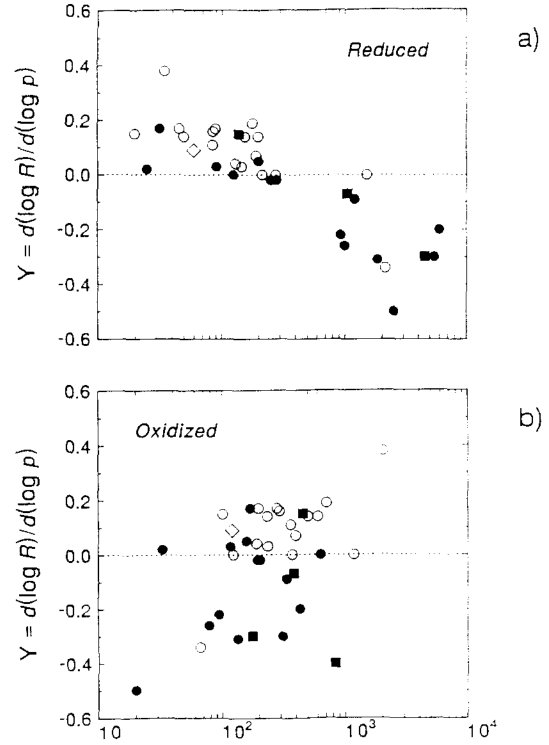

Fig. 7. Correlation between the gradient of resistivity change $Y \equiv \mathrm{d}\log[\rho(300\ \mathrm{K})]/\mathrm{d}\log[p(O_2)]$ and the room-temperature resistivity $\rho(300\ \mathrm{K})$ after: (a) reduction at 300°C and $p(O_2) = 0.0001$ atm; (b) oxidation at 300°C and $p(O_2) = 1.0$ atm. Closed circles: $X \leqslant 0.2$. Open circles: $0.2 < X < 0.6$. Squares: $X \geqslant 0.6$. Diamond: co-deposited $Sr_{0.9}CuO_{2-\delta}$ film. X is the (001)/(002) X-ray diffraction intensity ratio.

films. The situation is reversed in Fig. 7(b), after oxidation, although in this case it is remarkable that nearly all resistivities fall within the narrow band ~0.1–0.6 Ω cm. Considering the much larger resistivity range after reduction, this coalescence after oxidation is probably coincidental. As indicated by the different symbols, the different doping characteristics apparently correlate with the (001)/(002) intensity ratio. In particular, the closed circles in Fig. 7 indicate films for which $X \leqslant 0.2$. It follows that nearly all hole-doped films belong to this category. Conversely, not all films with $X \leqslant 0.2$ were hole-doped: For several films with small X the resistivity was nearly independent of the oxygen pressure ($Y \approx 0$).

The distinction between these two film types correlates with a difference in the deposition history: Invariably the hole-doped films with $X \leqslant 0.2$ were grown with Sr–CuO deposition sequences which may be characterized as "non-periodic," whereas "periodic" deposition sequences were used for the films with $Y \approx 0$. Hole-doped behavior also was observed for films with $X > 0.6$. On the other hand, nearly all films exhibiting $0.2 < X < 0.6$ (open circles) appeared electron-doped with $Y \approx 0.1$–0.2. A large majority of these electron-doped films were grown with "periodic" Sr–CuO deposition schemes. The systematic distinction with respect to doping characteristics, X-ray diffraction peak intensity ratio, and deposition history suggests a systematic correlation with different defect structures, which we shall discuss in the following section.

5. Charge doping model and correlations with layer-by-layer growth process

The gradients Y have been plotted against the (001)/(002) intensity ratios X in Fig. 8, together with a plausible model for the defect structures involved. In this model we have made the simplifying assumption that the observed doping phenomena can be described with essentially two defect types, namely

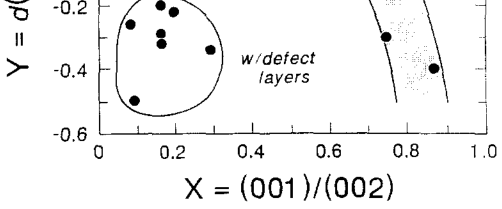

Fig. 8. Correlation between the gradient of resistivity change $Y \equiv \mathrm{d}\log[\rho(300\ \mathrm{K})]/\mathrm{d}\log[p(O_2)]$ and the (001)/(002) X-ray diffraction intensity ratio X for infinite layer $Sr_{1-x}CuO_{2-\delta}$ films grown with periodic and non-periodic layering schemes. Closed circles: hole-doped films ($Y \leqslant -0.05$). Open circles: electron-doped films ($Y \geqslant 0.05$) and films exhibiting weak variation of the resistivity with $p(O_2)$ ($|Y| < 0.05$). Diamond: co-deposited $Sr_{0.9}CuO_{2-\delta}$ film. Areas indicate films with assumed corresponding defect structures.

point defects leaving the basic four-fold Cu–O coordination intact, and planar type intergrowths containing oxygen atoms with apical Cu–O coordination towards adjacent CuO_2 sheets. Furthermore, in accordance with structure relations for the known superconducting cuprates, we assume that four-fold coordinated CuO_2 sheets can be doped with electrons and that at least a five-fold Cu–O coordination is required for hole doping. Thus we infer that the hole-doped, "non-periodic" films contain planar defect layers (most likely SrO_{1-x}), and that the wide range of diffraction intensity ratios observed for the electron-doped, "periodic" films results primarily from Sr point defects. With this simple model all the trends presented in the previous section can be rationalized.

The doping characteristics for the "periodic" films can be explained as follows: At low Sr defect densities ($X<0.2$), limited oxygen vacancies are available for oxygen exchange, and the induced carrier density (resistivity) does not depend strongly on the oxygen pressure ($Y\approx 0$). At greater defect densities ($X>0.2$) more oxygen vacancies are induced in the CuO_2 planes (to preserve local charge neutrality), giving rise to a stronger dependence of the resistivity on $p(O_2)$ and to electron doping. Takano et al. [17,31] argued that, in $Sr_{1-x}CuO_{2-\delta}$ and other (AE)CuO_2 compounds with large average AE ion radius, large interfacial stresses may be present as a result of (AE)–O and Cu–O bond length mismatch. Being tensile for the CuO_2 sheets and compressive for the oxygen depleted AE layers, these interplanar stresses are considered the main cause for metastability of the infinite layer structure. The stresses may be relaxed by the injection of electrons into the CuO_2 sheets [3], or the introduction of Sr vacancies to reduce the average ion size. It appears therefore that the observed tendencies towards electron doping and Sr deficiency in the same films represent natural tendencies of the infinite layer $Sr_{1-x}CuO_{2-\delta}$ structure, both originating from the same structural mismatch.

The Sr vacancies, however, counteract the electron doping of the CuO_2 sheets, which may ultimately be responsible for the absence of superconductivity in these $Sr_{1-x}CuO_{2-\delta}$ thin films. The introduction of Sr vacancies provides a relief mechanism for the tensile stress on the CuO_2 sheets, which would tend to reduce the number of injected electrons. Moreover, the positive charge associated with each Sr point defect may reduce the mobile carrier density. Unlike the rare earth-doped bulk materials [14–16], which apparently contain a stoichiometric (Sr+RE):Cu ratio [32], the net sheet electron density in the $Sr_{1-x}CuO_{2-\delta}$ films may be insufficient to induce superconductivity. Oxygen vacancies incorporated in the CuO_2 sheets to neutralize the positive charge of the Sr vacancies may further reduce the volume fraction of material capable of becoming superconducting. Possibly, the energy barrier for Sr point defect formation during layer-by-layer film growth is lower than that during high-pressure sintering. A variable Sr:Cu composition then may have resulted in the present work for the "periodic" films because of subtle differences in the Sr:Cu composition of atoms migrating on the film surface.

Preliminary results from Hall measurements on one of the "periodic" films assumed to contain Sr vacancies confirm the negative carrier density. The negative Hall carrier density increases with decreasing oxygen content (pressure), consistent with the positive sign of Y. In addition to the tensile stress on the CuO_2 planes, therefore, oxygen vacancies also may contribute to the negative sign of the majority charge carriers. In the case of $Sr_{1-x}CuO_{2-\delta}$ films on $SrTiO_3$ substrates, the tendencies towards Sr deficiency and electron doping may be further influenced by the slightly undersized substrate lattice parameter. A negative Hall carrier density also was measured for several of the co-deposited $Sr_{1-x}CuO_{2-\delta}$ films recently reported by Norton et al. [25].

The sudden changeover from electron doping to hole doping for the "periodic" films with $X>0.7$ suggests a drastic change in the defect structure. Possibly the Sr vacancies cluster into defect layers as described by Hiroi et al. [18]. Although the mechanism by which the hole doping emanates from the proposed $Sr_{1-\Delta}$–$CuO_{2-\delta}$–$Sr_{1-\Delta}$ "charge reservoir" layers has not been clarified, one may speculate that the oxygen substructure has rearranged such that apical oxygen atoms are present in the $Sr_{1-\Delta}$ layers adjacent to unperturbed CuO_2 sheets. An estimate of the Sr deficiency for the films with $X>0.7$, without taking into account possible phase shifts from planar defects, yields $x\approx 0.3$–0.35, i.e. close to the stability limit for $Sr_{1-x}CuO_{2-\delta}$ films [25].

In the case of the "non-periodic" films we consider SrO_{1-x} intergrowth layers the most likely cause for the observed hole-doping characteristics. As noted in section 2, extra depositions of CuO during the layer-by-layer growth rapidly lead to the formation of phase-segregated, copper-rich islands on the film surface, which apparently do not react with subsequently deposited Sr atoms to form $Sr_{1-x}CuO_{2-\delta}$. By contrast, extra Sr deposition, while not completely wetting the underlying surface, "neutralizes" with subsequent CuO supply to produce again a flat surface and, apparently, continued growth of the infinite layer structure. A reduced Sr deficiency for the "non-periodic" films also is indicated by the relatively small (001)/(002) intensity ratios $X<0.2$. Therefore, we assume that the defect structure for films with extra Sr(O) depositions is related to the superconducting "02($n-1$)n" phases recently proposed by Adachi et al. [22], containing double layers of SrO_{1-x} between blocks of the infinite layer phase with varying numbers n of CuO_2 sheets. Relatively little effect on the (001)/(002) intensity ratios is expected from this defect structure because the extra interplanar spacing associated with the double SrO_{1-x} layers corresponds to ~6.8 Å, i.e. approximately twice the infinite layer c-axis length.

A detailed examination of the relation between deposition history and defect formation is facilitated by Table 1, which summarizes the properties of selected films together with a brief description of the employed deposition schemes. In addition to films A and B featured earlier in this paper, three other layer-by-layer deposited films are listed, as well as a co-deposited Sr-deficient film (film F). Comparison with co-deposition growth techniques is interesting because in the latter case formation of the epitaxial structure is controlled entirely by spontaneous ordering processes at the film surface. Thus, film F was grown by laser ablation from a composite $Sr_{0.9}CuO_{2-\delta}$ target in the laser-MBE chamber, using the same deposition conditions as for the layer-by-layer films. The observed intensity ratio $X\approx0.14$ for this film agrees well with the calculated ratio for a 10% Sr-deficient lattice [25], suggesting that the film composition is nearly the same as that of the target. Consistent with the correlation of Fig. 8 for "periodic" films, film F exhibited moderate electron-doped behavior with $Y\approx0.09$.

Comparison between films C, D, and E illustrates the effects of deviations in the overlayer coverage and insertion of extra SrO_{1-x} defect layers. The extent of the overlayer coverage during each deposition cycle may be inferred from columns 3 and 4 indicating, respectively, the number of Sr–CuO deposition cycles supplied, and the number of $Sr_{1-x}CuO_{2-\delta}$ unit-cell layers formed. The number of $Sr_{1-x}CuO_{2-\delta}$ unit-cell layers was derived from the finite size interference

Table 1
Growth parameters and measured properties for selected infinite layer $Sr_{1-x}CuO_{2-\delta}$ films on (100) $SrTiO_3$ substrates. Indicated are, respectively, a global description of the layer-by-layer deposition scheme, the number of Sr–CuO deposition cycles, the number of $Sr_{1-x}CuO_{2-\delta}$ unit cell layers as inferred from X-ray diffraction, the (001)/(002) X-ray diffraction intensity ratio, the room-temperature resistivity ρ(300 K) after oxidation in 1.0 atm of oxygen and after reduction in 0.0001 atm oxygen, the gradient of the resistivity change after annealing at 300°C, and the c-axis lattice parameter after oxidation, reduction, or "as-grown" after cooling in 10^{-5} mbar NO_2 (indicated by brackets). Film F was grown by laser ablation from a composite $Sr_{0.9}CuO_{2-\delta}$ target. The asterisk at the (001)/(002) intensity ratio for film B indicates that the (001) peak for this film was split (see text)

Sample	General description	Number of cycles	Thickness (layers)	$\frac{(001)}{(002)}$	ρ(300 K) (mΩ cm)		$\frac{d(\log\rho)}{d[\log p(O_2)]}$	c(Å)	
					oxidized	reduced		oxidized	reduced
A	periodic	41	36	0.29	1990	35	+0.38	3.471	3.461
B	non-periodic	22+1 SrO +1 CuO	21	0.09 *	20	2500	−0.52	3.460	3.453
C	periodic (<ML)	43	23	0.30	311	86	+0.16	⟨3.465⟩	
D	periodic (>ML)	25	29	0.16	294	5400	−0.29	⟨3.454⟩	
E	non-periodic	52+5 SrO	29	0.16	134	1835	−0.30	⟨3.458⟩	
F	co-deposition [$Sr_{0.9}CuO_{2-\delta}$]	–	30	0.14	120	60	+0.09	⟨3.446⟩	

peaks in the θ–2θ X-ray diffraction pattern (see e.g. Fig. 5 for films A and B) taking into account the c-axis length [26]. Accordingly, Table 1 shows that the periodic overlayer coverage was less than 1 monolayer (ML) for films C and E, larger than 1 ML for film D, and approximately equal to 1 ML for films A, B. It is of interest to note that, although systematic variations in the overall RHEED pattern are observed regardless of the overlayer coverage, there is a clear distinction with respect to the quality of the intensity oscillations of the specularly reflected electron beam. While nearly undamped for overlayer coverages less than 1 ML (under optimized conditions), the oscillation amplitude decays rapidly for overlayer coverages larger than 1 ML. Practically this means that control of the growth process by monitoring of the induced variations in the RHEED pattern is more readily achieved for periodic sub-monolayer depositions than for overlayer depositions $\geqslant 1$ ML.

In the case of film C, the use of sub-monolayer depositions was deliberately exaggerated (giving rise to slowly damped RHEED oscillations) and the film became electron-doped with $Y \approx 0.16$, apparently accompanied by a sizable Sr deficiency ($x \approx 0.25$ from $X \approx 0.30$). Film C may be regarded as typical for the electron-doped "periodic" films of Fig. 8, except that for most of those films the overlayer coverage was chosen closer to 1 ML. On the other hand, film D, grown with Sr and CuO overlayer depositions periodically larger than 1 ML, became hole-doped with $Y \approx -0.29$. The contrast between films C and D suggests that the defect structure depends on the supplied overlayer coverage, apparently superimposed on the spontaneous tendency for formation of a Sr-deficient infinite layer structure. Assuming that growth of the infinite layer structure proceeds cell-by-cell (to preserve charge neutrality), the difference between films C and D can be explained in terms of a reduced mixing of constituents at the growth front(s) in case of the larger than monolayer depositions. On the other hand, sub-monolayer Sr and CuO depositions may promote surface diffusion conditions similar to those achieved during co-deposition, suggesting that the defect structure and physical properties of such films also should be similar. The similarities between the co-deposited film F and the trend for the "periodic submonolayer" films seems to confirm this speculation.

The effect of extra Sr depositions is illustrated by film E, grown in essentially the same "sub-monolayer" fashion as film C, except for the insertion of five extra SrO monolayers at non-uniform intervals in the stacking sequence. As indicated in Table 1, the extra Sr depositions rendered the film hole-doped with $Y \approx -0.30$, apparently overcompensating electron-doping contributions from the intermediate, and presumably Sr-deficient, infinite layer blocks. It seems likely that the microstructures of the films exhibiting a peaked resistivity dependence on $p(O_2)$ resemble that of film E, except for different distributions of the hole-doped and electron-doped areas in the film. On the other hand, the larger-than-average oxygen induced resistivity variations for films A and B indicate reduced compensating effects on the carrier density, suggesting that the electrical properties of these films are more closely dominated by only one defect type. As indicated in Table 1 the structural difference between these two films presumably resulted from the deposition of a single extra Sr(O) and a single extra CuO_x overlayer in the case of film B. The extra depositions produced a splitting of the (001) diffraction peak (peak positions at $2\theta \approx 24.7°$ and $26.0°$), indicating the existence of a superstructure along the surface normal [13]. Together with the effect of overlayer coverage, the widely different doping behavior for films A and B provides strong evidence for the different "infinite layer" microstructures which may result from adjustment of the layer-by-layer deposition scheme. Further research focusing on a comparison between co-deposition and layer-by-layer deposition schemes for $Sr_{1-x}CuO_{2-\delta}$ films is currently in progress to further delineate spontaneous and artificially imposed growth events.

6. Conclusions

The ability to engineer the defect structure of superconducting cuprate films via a layer controlled deposition process has been demonstrated for infinite layer $Sr_{1-x}CuO_{2-\delta}$ thin films on (100) $SrTiO_3$ substrates. Using independently controlled sources for the alternate deposition of Sr(O) and CuO_x monolayers and in situ RHEED to monitor the epitaxial overgrowth, it was confirmed that distinct defect structures may be introduced into the infinite layer cuprate structure by adjustment of the Sr–CuO deposition scheme. Films grown with different deposition schemes exhibited distinct doping mechanisms, as inferred from the electrical response to low-temperature oxygen exchange. Thus, the present study provides a baseline for future research, with identification of conditions leading to nearly stoichiometric $SrCuO_2$ films and conditions leading to the injection of electrons or holes into the $Sr_{1-x}CuO_{2-\delta}$ structure.

An interesting observation is the apparently natural tendency towards electron doping and Sr deficiency in the infinite layer $Sr_{1-x}CuO_{2-\delta}$ films, even without rare earth substitution. The electron-doping characteristics are observed most clearly for films grown with periodic Sr–CuO deposition sequences and also for co-deposited $Sr_{1-x}CuO_{2-\delta}$ films. Additionally, interesting phenomena were observed in the RHEED patterns which indicate that growth of the infinite layer cuprate structure under the employed deposition conditions may proceed cell-by-cell rather than strictly atomic layer-by-layer. A cell-by-cell growth mode also would be expected based on the charged nature of the CuO_2 and oxygen depleted AE lattice planes, neither of which is expected to be stable as lattice terminations in contact with an oxidizing gas ambient. It is plausible that the spontaneous Sr point defect incorporation is related to this cell-by-cell growth mode. In this scenario, statistical and kinetic effects at the crystalline growth front(s) may control the Sr defect incorporation.

With respect to the onset of superconductivity the present study suggests that hole doping via the intergrowth of SrO_{1-x} double layers forms a promising structural modification to introduce the necessary charge carriers into the infinite layer structure. Films containing extra Sr(O) depositions nearly always became hole-doped, despite the fact that the extra SrO_{1-x} overlayers did not optimally wet the underlying structure. It is likely that improvements in the formation of contiguous SrO_{1-x} defect layers may be realized by optimization of the growth conditions. Accordingly, it would be interesting to confirm the recent conclusions of Adachi et al. [22] and Hiroi et al. [23] with respect to the relation between superconductivity and the presence of SrO_{1-x} double layers in the infinite layer structure for films.

Finally, the present work indicates that the (defective) infinite layer $Sr_{1-x}CuO_{2-\delta}$ films exhibit a readily accessible processing range for reversible oxygen exchange. The possibility to study the properties of the infinite layer material at distinct oxygen contents may prove of great interest for further evaluation of the origin of its superconducting properties.

Appendix. Search for superconductivity

As indicated in Fig. 7 and Table 1, films A and B exhibited the strongest variations of the resistivity with oxygen pressure, the former being electron-doped, the latter hole-doped. The large gradients Y suggest that further lowering of the resistivity, perhaps leading to the onset of superconductivity, may be achieved for these films by further processing under the appropriate conditions. Accordingly, film A was repeatedly re-annealed in a vacuum chamber (base pressure $\sim 10^{-6}$ mbar) with heater temperatures eventually reaching 550°C (lower temperatures were used initially). However, the resistivity decreased by only a few percent and no significant changes were observed in the temperature dependence of ρ. Other electron-doped films with smaller gradients Y produced similar results, suggesting that either the surface temperature in vacuum remained too low or a saturation of the oxygen nonstoichiometry.

On the other hand, film B after annealing at a high oxygen pressure of ~ 160 atm (300°C, 1 h), exhibited a modest resistivity decrease and a faint anomaly in the temperature dependence of the four-probe resistance at 80–100 K (Fig. 9). The anomaly reproduced after remounting of the film the next day. Effects from uncompensated thermal voltages may be considered negligible at the relatively high measuring currents employed ($1\ \mu A \approx 30\ A/cm^2$), which is also borne out by the fact that no anomaly was observed for any of the other films exhibiting comparably low resistance values and slopes dR/dT over the same temperature interval. We therefore assume that the resistive anomaly of Fig. 9 represents a true sample phenomenon. We note that for film B only two extra defect layers were deposited; if only one or two defect layers were present in the film, the possibility exists that all of the electrical current was confined to only a few contributing CuO_2 sheets.

The hysteresis with respect to trapped magnetic flux

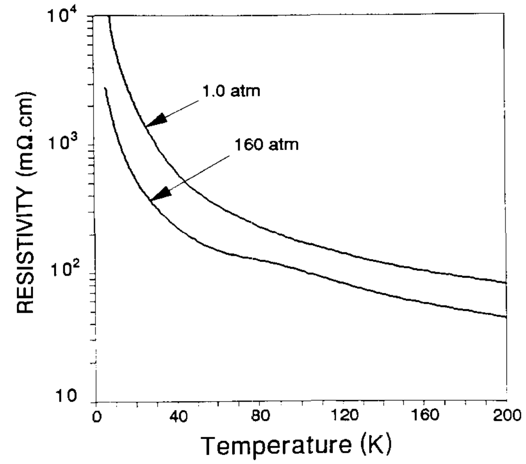

Fig. 9. Four-probe resistivity vs. temperature for film B after annealing at 300°C and the indicated oxygen pressures. The curve after annealing at $p(O_2) \approx 160$ atm exhibits a weak anomaly at 80-100 K.

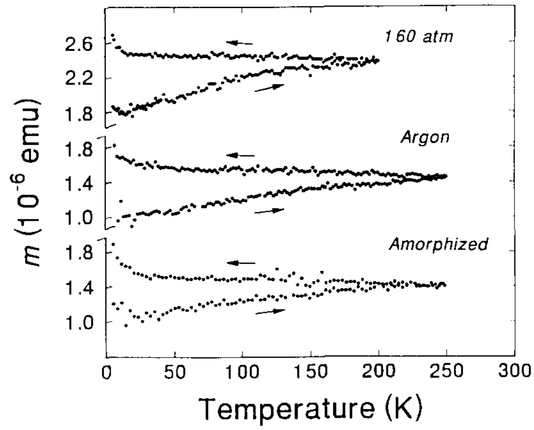

Fig. 10. Magnetic moment of film B on (100) $SrTiO_3$ substrate versus temperature in a magnetic field of 200 Oe applied in a direction 20° from the surface normal. The curves were obtained after annealing at 300°C at the indicated oxygen pressures and after amorphization by ion irradiation (bottom curve), respectively. Arrows indicate the sense of temperature variation, increasing for the zero-field-cooled curve and decreasing for the field-cooled curve.

was measured for film B using a Quantum Design MPMS-7 superconducting-quantum-interference-device (SQUID)-based magnetometer. The measurements were performed using an applied magnetic field of 200 Oe in a direction 20° from the surface normal (c-axis). Following the usual procedures, the film was first cooled to 5 K in the absence of a magnetic field. Then the field was turned on and the sample was heated to 200-250 K (ZFC-curve), after which the film was cooled again, this time in the presence of a magnetic field (FC-curve). The scan length in the SQUID magnetometer was set at 4 cm.

The results are shown in Fig. 10 for film B after high-pressure annealing (top curve), together with repeated measurements after further processing. Although fully oxygenated $SrTiO_3$ is diamagnetic [33], a clear paramagnetic moment is observed for the film-substrate combination. Additional experiments indicate that this paramagnetic moment *does not scale* with the film thickness, but rather varies from sample to sample and depends on the previous processing. A small but distinct hysteresis is observed in the temperature dependence of this paramagnetic signal, dependent on the field history. Both the kink at ~ 120 K (top curve) and the sign of the magnetic hysteresis are suggestive for the onset of superconductivity. However, as indicated by the other two curves of Fig. 10, the hysteresis persisted after a 300°C anneal in argon (giving rise to a 100-fold increase of the resistivity) and complete amorphization of the $Sr_{1-x}CuO_{2-\delta}$ film by ion irradiation (400 keV oxygen ions, dose 3×10^{15} cm^{-2}). Also, the magnitude of the paramagnetic background changed as a result of the reduction anneal.

The hysteresis remaining after amorphization effectively rules out a correlation with superconductivity for any of the magnetization curves of Fig. 10. Consequently, the information provided by the magnetization data with respect to the resistive anomaly of Fig. 9 is inconclusive. Although a significantly smaller hysteresis was observed for a fresh $SrTiO_3$ substrate (that was diamagnetic), it nevertheless seems likely that the hysteresis observed in Fig. 10 is related to the known ~ 100-K structural phase transition of the substrate. Observation supporting this view is the existence of a correlation between the magnitude of the ZFC-FC hysteresis and the magnitude of the paramagnetic background signal, as observed for different film-substrate combinations. Possibly, the paramagnetic background signal results from a variable oxygen deficiency of the substrate [33], however, little if anything has been published in recent years concerning a magnetic hysteresis for $SrTiO_3$. We conclude that for sample geometries and masses similar to those employed here, a practical underlimit of ~ 10^{-5} emu should be observed to infer the existence of superconductivity from hysteretic magnetization measurements for cuprate films on $SrTiO_3$.

Finally we note that several other (hole-doped) films decomposed as a result of the high-pressure anneal. Further research is desirable to establish the (kinetic) phase stability limits of the $Sr_{1-x}CuO_{2-\delta}$ infinite layer compound series under different temperature–oxygen pressure conditions.

Acknowledgements

The authors are indebted to R.K. Williams (Metals and Ceramics Division, ORNL) for performing the high-pressure oxygen anneals and D.K. Thomas (Surface Modification and Characterization Facility, ORNL) for assistance with the ion irradiation experiment. RF wishes to thank the staff and students at Osaka University for their generous hospitality and helpful assistance during his stay in Japan. This research was sponsored in part by the Japan Society for the Promotion of Science under its 1992 Fellowship Program, and the Division of Materials Sciences, US Department of Energy under contract No. DE-AC05-84OR21400 with Martin Marietta Energy Systems, Inc. Part of this research was performed at the ORNL PRT Beamline X-14 at the National Synchrotron Light Source, Brookhaven National Laboratory.

References

[1] T. Siegrist, S.M. Zahurak, D.W. Murphy and R.S. Roth Nature 324 (1988) 231.

[2] R.J. Cava, Nature 351 (1991) 518.

[3] J.B. Goodenough and A. Manthiram, J. Solid State Chem. 88 (1990) 115.

[4] Y. Tokura, Physica C 185–189 (1991) 174.

[5] T. Wada, A. Ichinose, H. Yamauchi and S. Tanaka, Physica C 185–189 (1991) 729.

[6] H. Nobumasa, K. Shimizu and T. Kawai, Z. Phys. B 83 (1991) 7.

[7] M. Takano, Y. Takeda, H. Okada, M. Miyamoto and T. Kusuka, Physica C 159 (1989) 375.

[8] M. Kanai, T. Kawai and S. Kawai, Appl. Phys. Lett. 58 (1991) 771.

[9] X. Li, M. Kanai, T. Kawai and S. Kawai, Jpn. J. Appl. Phys. 31 (1992) L217.

[10] H. Adachi, T. Satoh, K. Setsune and K. Wasa, Physica C 196 (1992) 14.

[11] C. Niu and C.M. Lieber J. Am. Chem. Soc. 115 (1993) 137.

[12] D.P. Norton, B.C. Chakoumakos, J.D. Budai and D.H. Lowndes, Appl. Phys. Lett. 62, 1679 (1993).

[13] M. Kawai, Z. Liu, R. Sekine and H. Koinuma, Jpn. J. Appl. Phys. 32, 1208 (1993).

[14] M.G. Smith, A. Manthiram, J. Zhou, J.B. Goodenough and J.T. Markert, Nature 351, 549 (1991).

[15] G. Er, Y. Miyamoto, F. Kanamaru and S. Kikkawa, Physica C 181, 206 (1991).

[16] N. Ikeda, Z. Hiroi, M. Azuma, M. Takano, Y. Bando and Y. Takeda, Physica C 210, 367 (1993).

[17] M. Takano, M. Azuma, Z. Hiroi, Y. Bando and Y. Takeda, Physica C 176, 441 (1991).

[18] Z. Hiroi, M. Takano, M. Azuma, Y. Takeda and Y. Bando, Physica C 185–189, 523 (1991).

[19] M. Azuma, Z. Hiroi, M. Takano, Y. Bando and Y. Takeda, Nature 356, 775 (1992).

[20] S. Adachi, H. Yamauchi, S. Tanaka and N. Mori, Physica C 208, 226 (1993).

[21] Z. Hiroi, M. Azuma, M. Takano and Y. Takeda, Physica C 208, 286 (1993).

[22] S. Adachi, H. Yamauchi, S. Tanaka and N. Mori, Physica C 212, 164 (1993).

[23] Z. Hiroi, M. Takano, M. Azuma and Y. Takeda, Nature 364, 315 (1993).

[24] T. Matsumoto, T. Kawai, K. Kitahama, S. Kawai, I. Shigaki and Y. Kawate, Appl. Phys. Lett. 58, 2039 (1991).

[25] D.P. Norton, B.C. Chakoumakos, E.C. Jones, D.K. Christen and D.H. Lowndes, Physica C 217, 146 (1993).

[26] T. Terashima, Y. Bando, K. Iijima, K. Yamamoto, K. Hirata, K. Hayashi, K. Kamigaki and H. Terauchi, Phys. Rev. Lett. 65, 2684 (1990).

[27] R. Feenstra, D.K. Christen, C.E. Klabunde and J.D. Budai, Phys. Rev. B 45, 7555 (1992).

[28] E.M. Carron III, M.A. Subramanian, J.C. Calabrese and R.L. Harlow, Mater. Res. Bull. 23, 1355 (1988).

[29] H. Müller-Buschbaum, Angew. Chem. Int. Ed. Engl. 16, 674 (1977);
C.L. Teske, H. Müller-Buschbaum, Z. Anorg. Allg. Chem. 371, 325 (1969).

[30] X. Li, T. Kawai and S. Kawai, Jpn. J. Appl. Phys. 31, L934 (1992).

[31] M. Takano, Z. Hiroi, M. Azuma and Y. Takeda, Jpn. J. Appl. Phys. Ser. 7 Mechanisms of Superconductivity (1992) p. 3.

[32] J.D. Jorgensen, P.G. Radaelli, D.G. Hinks, J.L. Wagner, S. Kikkawa, G. Er and F. Kanamaru, Phys. Rev. B 47, 14654 (1993).

[33] H.P.R. Frederikse and G.A. Candela, Phys. Rev. B 147, 583 (1966).